The Journal of Experimental Biology 203, 3733–3744 (2000)
Printed in Great Britain © The Company of Biologists Limited 2000
JEB2825

GLIDING FLIGHT: DRAG AND TORQUE OF A HAWK AND A FALCON WITH STRAIGHT AND TURNED HEADS, AND A LOWER VALUE FOR THE PARASITE DRAG COEFFICIENT

VANCE A. TUCKER*

Department of Biology, Duke University, Box 90338, Durham, NC 27708-0338, USA

*e-mail: vtucker@duke.edu

Accepted 25 September; published on WWW 14 November 2000

Summary

Raptors – falcons, hawks and eagles in this study – such as peregrine falcons (*Falco peregrinus*) that attack distant prey from high-speed dives face a paradox. Anatomical and behavioral measurements show that raptors of many species must turn their heads approximately 40 ° to one side to see the prey straight ahead with maximum visual acuity, yet turning the head would presumably slow their diving speed by increasing aerodynamic drag. This paper investigates the aerodynamic drag part of this paradox by measuring the drag and torque on wingless model bodies of a peregrine falcon and a red-tailed hawk (*Buteo jamaicensis*) with straight and turned heads in a wind tunnel at a speed of 11.7 m s^{-1}. With a turned head, drag increased more than 50 %, and torque developed that tended to yaw the model towards the direction in which the head pointed. Mathematical models for the drag required to prevent yawing showed that the total drag could plausibly more than double with head-turning. Thus, the presumption about increased drag in the paradox is correct.

The relationships between drag, head angle and torque developed here are prerequisites to the explanation of how a raptor could avoid the paradox by holding its head straight and flying along a spiral path that keeps its line of sight for maximum acuity pointed sideways at the prey. Although the spiral path to the prey is longer than the straight path, the raptor's higher speed can theoretically compensate for the difference in distances; and wild peregrines do indeed approach prey by flying along curved paths that resemble spirals.

In addition to providing data that explain the paradox, this paper reports the lowest drag coefficients yet measured for raptor bodies (0.11 for the peregrine and 0.12 for the red-tailed hawk) when the body models with straight heads were set to pitch and yaw angles for minimum drag. These values are markedly lower than value of the parasite drag coefficient ($C_{D,par}$) of 0.18 previously used for calculating the gliding performance of a peregrine.

The accuracy with which drag coefficients measured on wingless bird bodies in a wind tunnel represent the $C_{D,par}$ of a living bird is unknown. Another method for determining $C_{D,par}$ selects values that improve the fit between speeds predicted by mathematical models and those observed in living birds. This method yields lower values for $C_{D,par}$ (0.05–0.07) than wind tunnel measurements, and the present study suggests a value of 0.1 for raptors as a compromise.

Key words: flight, gliding, drag, torque, red-tailed hawk, *Buteo jamaicensis*, peregrine falcon, *Falco peregrinus*, visual acuity.

Introduction

This paper reports the aerodynamic drag and torque on wingless model raptor bodies with their heads in two positions: straight, or turned 40 ° to the right. The aerodynamics of turned heads in raptors – falcons, hawks and eagles in this study – is interesting, because these birds have three properties that seem to be in conflict. (i) Some raptors, particularly large falcons such as peregrines (*Falco peregrinus*), approach prey by diving at it from great distances at high speeds. (ii) The aerodynamic drag on raptor bodies is presumably minimal for given conditions when their body is symmetrical, i.e. when the head is straight rather than turned to one side. (iii) Raptors appear to have their most acute vision along a line of sight directed approximately 40 ° to either side of the head axis. So how can a raptor approach prey at high speed if it must turn its head sideways to see distant prey straight ahead, thereby increasing drag?

The present paper is the first of a series of three that investigate this conflict. It quantifies the dependence of drag on head angle in body models of a peregrine falcon (PF) and a red-tailed hawk (RT, *Buteo jamaicensis*). The second paper (Tucker, 2000) shows that raptors look almost exclusively sideways rather than straight at objects more than 40 m away. It also shows that raptors could approach prey by flying along a spiral path that keeps their line of sight for maximum visual

acuity pointing sideways at the prey while their heads are straight for maximum speed. If they flew along a straight path, they would have to turn their heads to one side and fly slower to see the prey with maximum acuity. A higher speed could theoretically compensate for a longer spiral path and allow the raptor to reach the prey in the same time along either path. The relationship between drag and head angle established in the present paper is a prerequisite to this conclusion. The third paper (Tucker et al., 2000) shows that wild peregrines follow curved paths towards distant prey more often than straight ones. The curved paths resemble the spiral path that would allow the falcon to keep its head straight while viewing the prey to one side with maximum visual acuity.

The present paper also suggests that raptors with straight heads may have a lower parasite drag coefficient than the previously measured value (Tucker, 1990a). The model bodies in this study had the lowest drag coefficients yet measured for raptors, and a low parasite drag coefficient is consistent with speed measurements on a diving gyrfalcon (*Falco rusticolus*) (Tucker et al., 1998). Recent measurements on flapping birds also suggest lower values for parasite drag coefficients (Pennycuick et al., 1996).

Materials and methods

The PF and RT body models were mounted in a wind tunnel with two head positions: 'straight' models were bilaterally symmetrical with heads that pointed straight ahead, and 'bent' models had turned heads that pointed 40 ° to the right. The models had two characteristics essential for this study: (i) their shapes accurately replicated those of the real bird bodies, and (ii) except for head position, the straight and bent models had identical shapes. The following sections describe in detail the processes for measuring frozen bird bodies, making the models from the measurements and measuring drag and torque. Table 1 shows the accuracy of the measurement and model-making procedures.

The coordinate system and surface points

Both the measurement process and the model-making process used a large number of three-dimensional 'surface points' on a body or model to define shape. Each point has three values (z, r and the angle Θ) that describe it on a system of cylindrical coordinates. This system can be visualized relative to a cylinder with an axis along the z-axis and radii that extend perpendicularly in all directions from any point on the z-axis. Any point on the surface of the cylinder lies on a radius and is a distance r from the z-axis along that radius. The angle Θ identifies the radius, and a value for Θ alone identifies one of an infinite number of planes that contain the z-axis.

For the bird bodies and models described here, the body exclusive of the neck and head is bilaterally symmetrical; and the body axis, which is also the z-axis, runs from anterior to posterior in the midsagittal plane. Θ has a value of 0 ° for a 'ventral radius' that runs ventrally from the z-axis in the midsagittal plane and a value of 180 ° for a 'dorsal radius' that runs dorsally. 'Intermediate radii' run between the ventral and dorsal radii.

Table 1. *Accuracy of measurement procedures*

Quantity	Bias	Precision
Air speed ($m\,s^{-1}$)	0.02	0.01
Drag (N)	N	0.0015
Torque (N m)	N	0.001
Measured surface points (m)	N	0.0001
Armature surface points		
z (m)	N	0.0001
r (m)	N	0.00045
Θ (degrees)	N	0.1
Pitch and yaw angles (degrees)	N	0.15

Bias is the absolute difference between the mean measured value and the true value.

N indicates that the bias is negligible, i.e. less than one-quarter of the precision. Precision is the standard deviation of repeated measurements of a constant quantity.

Values of z vary in steps from the base of the beak to the base of the tail, and each value of z identifies a cross section ('section', for short) of the bird or model body. For example, a typical model body might have 40 sections, each with 20 radii, for a total of 800 surface points. These points define the 'armature' for the model, and the armature becomes the finished model after turning its head in bent models and smoothing its surface with a thin layer of plaster.

The armatures are bilaterally symmetrical, because the surface points on only one side of the armature come from measurements on frozen bodies. In the example above, only 11 of the 20 points in each section would be measured: the two points on the ventral and dorsal radii and the nine points on the intermediate radii for angles between 0 ° and 180 °. The remaining nine points fall on the intermediate radii between 180 ° and 360 ° and are reflections of the measured points.

Measurements from frozen bodies

I measured surface points on the frozen bodies of a PF (intact mass 0.713 kg) and an RT (intact mass 1.017 kg) after cutting off the wings at mid-humerus to leave the proximal humeral feathers attached to the body. These feathers smoothly covered the stump of the humerus (which was folded back parallel to the body surface) and the region where the wing had joined the body. I preened and smoothed the feathers on the slightly thawed bodies, as described in Tucker (1990a).

A digitizer connected to a computer recorded the coordinates of surface points on the feathers on one side of a frozen body, as described in Tucker (1990a). The PF had 46 sections spaced at 7.93 mm intervals and 6–31 measured surface points per section, depending on the size and shape of the section. The RT had 32 sections spaced at 12.70 mm intervals and 11 measured surface points per section. For the RT, these points fell on radii with steps of 18 ° between them, i.e. the ventral and dorsal radii and the nine intermediate radii. For both the

PF and the RT, the first section was at the base of the beak, and the last section was at the base of the tail.

The surface points for the PF were the same as those used by Tucker (1990a), but here they were used in each section to interpolate a new set of surface points that fell on the same radii described for the RT.

The armature-cutting (AC) machine

The AC machine cut model armatures from expanded polystyrene plastic (known as styrofoam) by using a hot wire to melt, or 'cut', an open channel (the kerf) through a styrofoam cylinder with a density of 16 or 32 kg m^{-3}. This cylinder was 0.13 m in diameter and up to 0.2 m long, depending on the size of the finished model, and its axis was the *z*-axis of the armature. The armature could be up to 0.4 m long, because the AC machine made the armature in separate anterior and posterior parts.

The AC machine cut an armature by a process somewhat like sharpening a pencil with a knife. The AC machine could rotate a plate, and I used hot wax to stick one end of the styrofoam cylinder to the plate so that the *z*-axis, the axis of the cylinder and the axis of rotation were all the same. The AC machine could then rotate the plate and the cylinder as one rotates a pencil while sharpening it. With the plate held at some value of Θ, the AC machine moved the a hot wire (the knife) from one end of the cylinder to the other along a curve in the plane for that value of Θ and sliced off a thin piece of styrofoam (the pencil shaving). The surface points for that value of Θ determined the shape of the curve. The AC machine then rotated the cylinder to the next value of Θ and moved the hot wire along another curve to slice off another thin piece of styrofoam. After several rotations through the set of 20 values of Θ, the hot wire had sliced off enough styrofoam to make the armature, just as a knife makes the pencil point by removing shavings.

The AC machine used computer-controlled stepping motors to rotate the cylinder and move the hot wire along the curve at a rate of approximately 5 mm s^{-1}. The wire, made from nichrome 0.13 mm in diameter and 95 m long, was perpendicular to the plane for Θ and carried a current of 0.6 A at 5.6 V. The wire moved through the styrofoam with virtually no mechanical resistance as it melted a kerf 0.4 mm wide. When the wire reached one end of the cylinder, the slice of styrofoam fell free, and the stepping motor rotated the cylinder to the next value of Θ. The AC machine then cut off the next slice of styrofoam as it moved the hot wire back to the other end of the cylinder, again along a specified curve. After 20 rotations, Θ was back where it started, and the AC machine repeated the process until it had cut the cylinder down to the armature. The AC machine typically made four cuts for each value of Θ, and took 100 min to finish both parts of the armature.

The computer program that controlled the stepping motors used the surface points in several calculations to determine the path of the hot wire in the plane for a given value of Θ. For example, the program decided how deep each cut could be, and checked the sequence of cuts for both previous and subsequent values of Θ to avoid interference between cuts (described in the next section). It also computed the combination of *z* and *r* steps that gave the shortest path between surface points on adjacent sections, and it scaled the surface points to make the armature a particular size.

The stepping motors moved the hot wire in 0.25 mm steps along the *z* axis, in 0.18 mm steps along the *r* axis and in 0.2 ° steps around the *z*-axis for Θ. The computer program used the length of the maximum radius for a surface point as a measure of armature size and scaled all the armatures so that this radius had a length of 55.9 mm. This value made the PF armature life size and the RT armature 0.87 times life size.

Finishing the armatures

I glued the anterior and posterior parts of an armature together with water-soluble glue, drilled a hole through the armature and glued a hardwood dowel into the hole. The hole was 9.5 mm in diameter and passed through the armature in the midsagittal plane near the middle of the sternum and parallel to the dorsal and ventral radii. The dowel served as a mount for the model in the wind tunnel, and a hole drilled along its axis received a threaded rod from the strut of the drag and torque balances. The strut ended flush with the ventral surface of the model, and a flush cap plugged the 9.5 mm hole on the dorsal side of the model. The distances from the base of the beak to the mounting strut were 0.152 m and 0.143 m for the PF and RT models, respectively.

The hot wire of the AC machine left the armature with a facetted surface (Fig. 1), and the ridges between the facets established the approximate surface of the finished model. The wire also fluffed out the armature, because the wire could not move into concavities on the perimeter of a section without cutting short the radii adjacent to the concavity. i.e. interfering with them (Fig. 1). The program that ran the AC machine recognized concavities and prevented such interference.

I coated the armature with a thin layer of plaster to round out the facets and sanded the model to its final shape. Next, I cut a beak and tail from styrofoam with a hot wire, glued them to the model, filled any crevices with plaster and sanded these appendages to their final shape. The result was a smooth model with a symmetrical body and surface roughness approaching that of a smooth plaster wall. The mass of the finished models was between 0.034 and 0.051 kg.

To turn the head on an armature, I cut two 20 ° wedges from the right side of the neck so that the sharp edge of each wedge was parallel to the dorsal and ventral radii and in the midsagittal plane (Fig. 2). One sharp edge was at the point where the neck joined the head, and the other was where the neck joined the shoulder girdle. I sliced the head from the armature by cutting from the line where the sharp edge of the anterior wedge had been, to the left side of the neck, and sliced off a section of the neck with a similar cut for the posterior wedge. I then glued the head, neck section and wedges back onto the armature with the wedges on the left side of the neck, and used a hot wire to smooth the neck to natural contours.

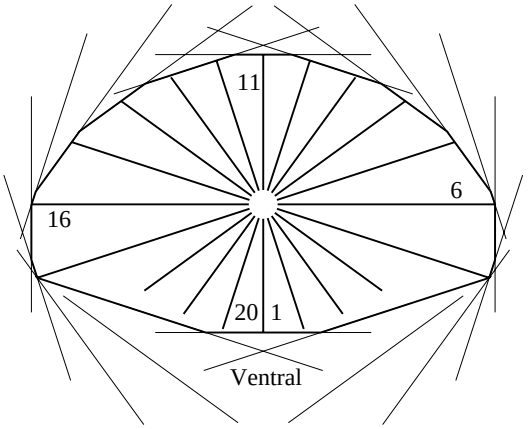

Fig. 1. A section of the styrofoam peregrine armature at the level of the bird's vent. The thick lines show two features: the perimeter of the section and the 20 radii (numbered from 1, counterclockwise) that radiate at 18 ° intervals from the *z*-axis to surface points. The thin lines show a 38.1 mm segment of the hot wire for each of the 20 cuts that finished the section. Each wire segment has an associated radius – the radius that it is near and perpendicular to. The wire ordinarily cuts at the end of its associated radius (e.g. the wire at the end of radius 1) but the program that controls the armature-cutting machine prevents it from doing so where there are concavities in the section perimeter, e.g. the concavity defined by the ends of radii 1–5. If the wire associated with radius 3, for example, made a cut at the end of radius 3, it would interfere with radii 4 and 5 by shortening them. The program prevents such interference and, as a result, the wire may not touch its associated radius (e.g. the wire positions associated with radii 2, 3, 4, 7, 8 and 9). The wire may also touch an associated radius for another wire position (e.g. the wire position associated with radius 4 touches radius 5) or may not touch any radius (e.g. the wire position associated with radius 3). The effect of interference prevention is that the armatures made by the armature-cutting machine have sections with filled-in concavities.

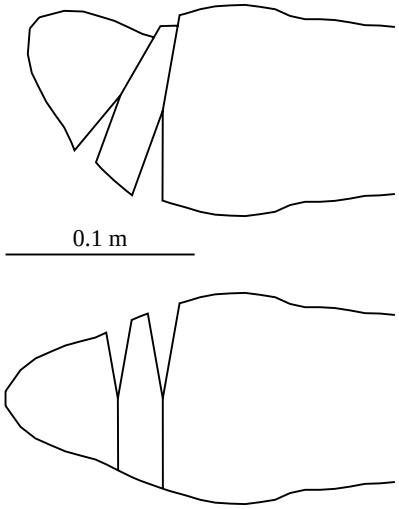

Fig. 2. A dorsal view of the anterior end of the styrofoam peregrine armature, showing the wedges removed and the cuts made to turn the head 40 ° to the right. The angle at the apex of each wedge is 20 °.

The result was a life-like armature with the head turned 40 ° to the right.

The laminated PF models

In addition to models cut from styrofoam, this study used the PF model described by Tucker (1990a). The armature of this model was made from plywood laminations shaped to fit the same surface points used to interpolate the surface points for the styrofoam PF armature cut by the AC machine. The model with the laminated armature – the laminated model – had a higher drag than the model with the styrofoam armature, but I was able to eliminate the difference by modifying the shape of the laminated model with plaster. This study discusses both the laminated model and the modified laminated model.

The wind tunnel, drag balance and torque balance

The wind tunnel (described by Tucker and Parrott, 1970) ran at a constant air speed (V) of 11.7 m s^{-1} in the region of the test section occupied by the body models. This value was measured with a pitot tube connected to a micromanometer and monitored by a digital counter that displayed the period between rotations of the wind tunnel fan shaft. The air density (ρ), temperature and atmospheric pressure during the measurements did not deviate significantly from 1.23 kg m^{-3}, 22 °C and 101.33 kPa (1 atmosphere), respectively, at sea level.

The drag balance (described in detail by Tucker, 1990b) was of the parallelogram type, with four strain gauges connected as a Wheatstone bridge cemented to the parallelogram arms. The voltage across the bridge, displayed by a digital voltmeter, was linearly related to the force component along the sensitive axis of the balance.

The torque balance was made by adding to the drag balance a vertical shaft that could rotate on low-friction ball bearings. The mounting strut for the models attached to the shaft and was approximately co-linear with it. The strut transmitted any torque around its axis to the shaft, and an arm on the shaft kept the shaft from rotating by pressing on the sensitive axis of the drag balance. With this arrangement, the voltmeter responded linearly to any torque produced by aerodynamic forces acting on the model.

The measurement procedure produced paired values of drag or torque, followed by calibration values. After mounting a model on the strut, I turned the wind tunnel on and recorded the voltmeter reading. Then I turned the tunnel off, waited for the wind speed to drop, turned the tunnel on again and recorded another voltmeter reading. With the tunnel off, I calibrated the balance by hanging weights on a thread attached to the strut of the drag balance or to the moment arm of the torque balance and running over a pulley on a low-friction ball bearing. The weights produced voltmeter readings that bracketed those for the model, and drag or torque were then calculated by interpolation.

This paper discusses both drag (D) and the drag coefficient (C_D):

$$C_D = 2D/(\rho S_b V^2), \quad (1)$$

where S_b is the area of the body model section with the largest area. C_D is a function of Reynolds number, which is proportional to S_b and V in this study. C_D often remains nearly constant for small changes in Reynolds number, but generally declines as Reynolds number increases (Tucker, 1987, 1998; Rayner, 1999). I shall assume that C_D is constant as a first approximation.

The mounting strut and interference drag

The mounting strut was 90 mm long from the top of the shroud of the drag balance to the surface of the model, and its cross-sectional shape was that of a Navy Number 1 strut (Tucker, 1990b). Its chord, from leading to trailing edges, was 6.2 mm, and its maximum thickness perpendicular to the chord was 2.5 mm. The strut was always aligned so that airflow in the wind tunnel was parallel to a line between its leading and trailing edges.

I calculated the drag of a model by subtracting strut drag and interference drag from the drag measured by the drag balance. Strut drag is the measured drag of the strut alone on the drag balance, and interference drag is drag that arises because of the mutual interference of the strut and the model with the airflow in the region where the strut attaches to the model. Interference drag in this study equals the strut drag multiplied by the ratio interference length/strut length, where interference length is 33.1 mm (Tucker, 1990b). The total of strut drag and interference drag was always less than 12 % of the drag measured by the drag balance.

Yaw and pitch angles of a model

The yaw angle is the angle between the direction of the *z*-axis and the direction of air flow in the wind tunnel, when both directions are projected onto a horizontal plane. The yaw angle is zero when the head of the model points directly upwind, and the angle increases when the *z*-axis rotates counterclockwise, as seen from above. A model could be set to any yaw angle by rotating it on the mounting strut.

The pitch angle is the angle between the direction of the *z*-axis and the direction of air flow in the wind tunnel, when both directions are projected onto a vertical plane. The pitch angle is zero when the yaw angle is zero and the model has minimum drag. The pitch angle increases when the *z*-axis rotates clockwise, as seen from the model's left side. A model could be set to pitch angles between –20 ° and 20 ° by rotating the mounting strut around the point where it attached to the drag or torque balance.

Nomenclature for models

This study discusses measurements on six models of bird bodies, and it also discusses mathematical models and torque models. Mathematical models are sets of equations, and torque models are mathematical models that calculate the drag required to generate torque. To distinguish these types of model, I shall henceforth refer to body models, mathematical models and torque models.

The body models include four made from styrofoam armatures cut by the AC machine: the straight PF, bent PF, straight RT and bent PF. The other two – the laminated model and the modified laminated model – are similar to the straight PF model.

Results

Drag coefficients of body models

The drag coefficients of body models depended on the species, on the pitch and yaw angles and on whether the model was straight, bent or laminated (Figs 3, 4). Table 2 gives equations for parabolas fitted by the least-squares method to the data. The following sections frequently describe the drag coefficient when the yaw and pitch angles are zero, and I shall use the symbol C_D for the drag coefficients measured under these conditions. In other cases, the text describes the measurement conditions for C_D.

Straight and bent models

The drag coefficients had three notable features. (i) The straight PF and RT models had C_D values of 0.11 and 0.12, respectively; both less than the previous lowest published value for a raptor (0.14, Tucker, 1990a). However, Nachtigall (1998) reports a lower value of 0.08 for a starling (*Sturnus vulgaris*). (ii) Turning the head 40 ° to the right increases the C_D values of both the PF and RT models by more than 50 % compared with their straight counterparts. (iii) C_D values are minimal for the bent PF and RT models when the models are yawed 7–10 ° in the direction opposite to that of the turned head.

Table 2. *Coefficients of parabolic equations fitted to parasite drag coefficients at various pitch and yaw angles*

	Angles		Parabolic coefficients		
Body model	Pitch	Yaw	C_1	C_2	C_3
Peregrine falcon, $S_b = 0.00669\ m^2$					
Straight	0	V	0.110	0	0.00011
Straight	V	0	0.111	–0.0002	0.00029
Bent	0	V	0.178	–0.0044	0.00024
Bent	V	0	0.172	–0.0001	0.00044
Laminated	V	0	0.134	–0.0020	0.00053
Red-tailed hawk, $S_b = 0.00785\ m^2$					
Straight	0	V	0.118	–0.0002	0.00016
Straight	V	0	0.120	0.0020	0.00037
Bent	0	V	0.171	–0.0061	0.00046
Bent	V	0	0.177	0.0028	0.00061

The parabolic coefficents are used in equations of the form $y=C_1+C_2x+C_3x^2$, where y is a parasite drag coefficient and x is the pitch or yaw angle of the model (in degrees).

The abbreviation V (variable) indentifies the angle to which x refers to, and the other angle is 0 °.

Figs 3 and 4 show the lines represented by these equations.

S_b is the cross-sectional area used to compute the parasite drag coefficient.

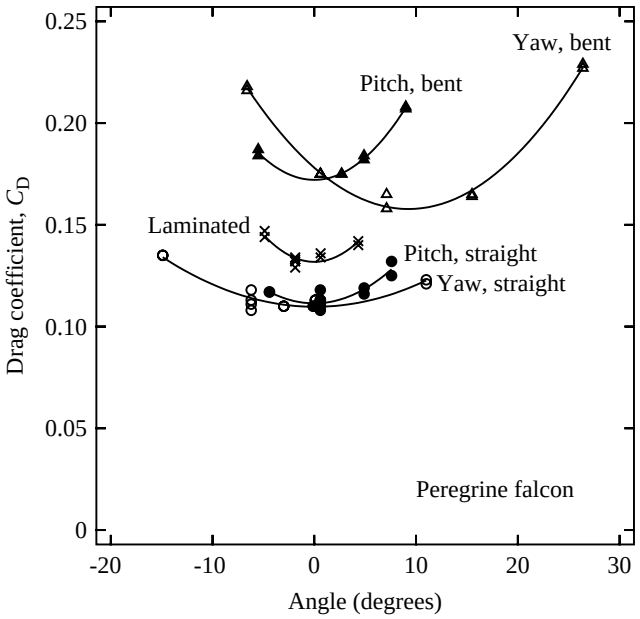

Fig. 3. The drag coefficients of the peregrine body (PF) models at different pitch or yaw angles. The points are in pairs and appear as a single point when they are identical. Table 2 gives the equations of curves fitted to these data.

Laminated PF models

The drag coefficients of the laminated and modified laminated models also have three notable features. (i) The laminated model in the present study has the same C_D as that found in a previous study of this model (Tucker, 1990a). (ii) The C_D for the laminated model is higher than that for the straight PF model, although both models were constructed

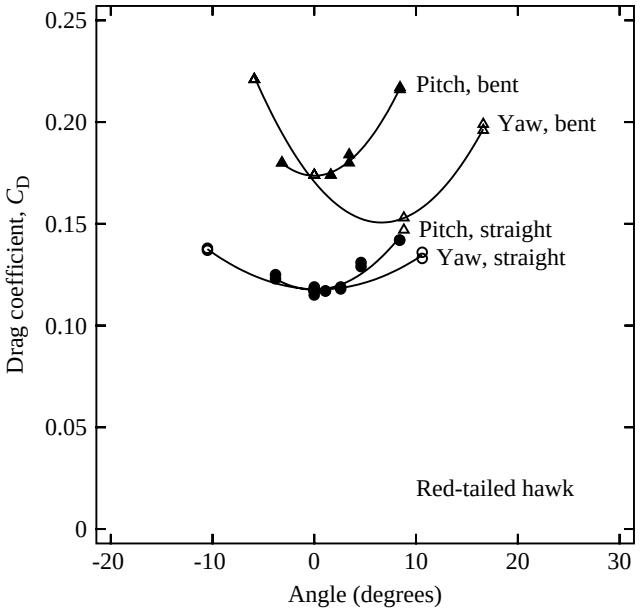

Fig. 4. The drag coefficients of the red-tailed hawk (RT) body models at different pitch or yaw angles. The points are in pairs and appear as a single point when they are identical. Table 2 gives the equations of curves fitted to these data.

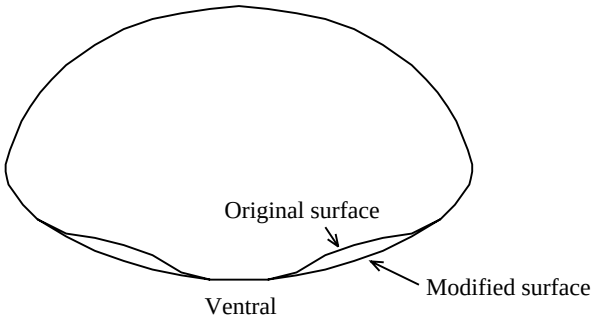

Fig. 5. A section of the laminated peregrine body model, superimposed on the same section from the modified laminated model. The modification consisted of adding plaster to fill in concavities in the surface of the laminated model. This section is the same section as that in Fig. 1 and shows added plaster 3 mm thick, the maximum thickness for any section.

using the same surface points (see above). The models looked similar, but careful examination showed that the AC machine introduced a difference into the armatures that it made: the sections of the armatures had no concavities in their perimeters, while the laminated model had shallow concavities on the perimeters of some of its sections (Fig. 5). In fact, the laminated model had concavities that ran lengthwise for several sections where the concavities of adjacent sections were in register. (iii) Filling in the concavities of the laminated model with plaster reduced its C_D to that of the straight PF model. I added plaster in two steps: the first step filled in the concavities posterior to the shoulder region, and the second step filled in those anterior to the shoulder region. The first filling reduced the difference between the C_D values of the straight PF and laminated models by two-thirds, and the second filling eliminated the remaining difference.

The largest and deepest concavities were around the thighs and in the vicinity of the vent, where the added plaster was up to 3 mm thick (Fig. 5). Evidently, lengthwise concavities on the body of a bird can markedly increase drag.

Torque on the bent body models

The bent models of both the PF and the RT developed substantial torque to the right at pitch and yaw angles of 0 °, and this torque increased rapidly when the model yawed towards its right (decreasing yaw angle) (Fig. 6). The torque decreased when the model yawed to its left, and became 0 ° at approximately the same angles where C_D was minimal for bent models (Figs 3, 4).

Discussion

The ideal falcon and drag partitions

The body models in this study have lower drag coefficients than those measured previously for raptors, and turning the head on a model markedly increases drag. What are the consequences of these findings for a gliding raptor? The drag on the body is only one component of the aerodynamic force

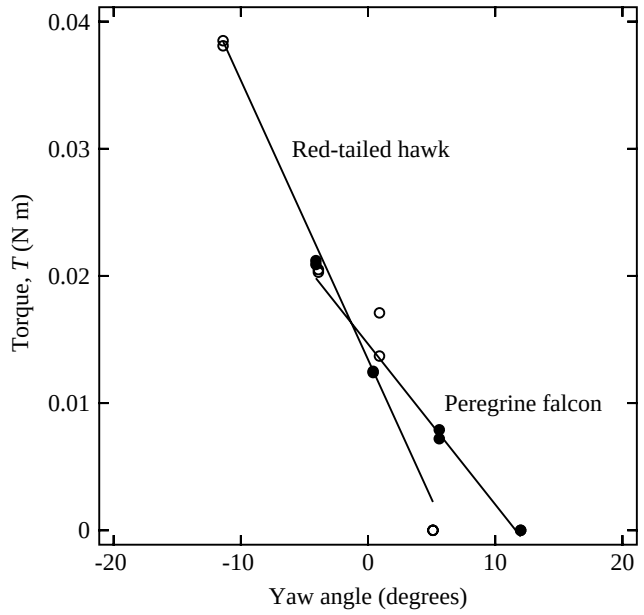

Fig. 6. The relationships between yaw angle and torque for the peregrine and red-tailed hawk body models with turned heads and pitch angles of 0 °. Points are in pairs and appear as a single point when they are identical. The equations for the fitted lines are T=0.01465–0.001262x for the peregrine, and T=0.01342–0.002195x for the red-tailed hawk, where x is the yaw angle in degrees.

on a flying bird, and the answer to this question requires the analysis of several other properties of the bird. To introduce these properties, I shall use the concept of an 'ideal falcon' (Tucker, 1998), which is an abstract falcon with mathematically defined morphological and aerodynamic properties. The name comes from the similarity between an ideal falcon and the 'ideal gas' of physical chemistry. Both are simplified, mathematically defined abstractions of their real counterparts, yet they represent reality closely enough to provide an understanding of how their counterparts behave.

The mathematical model for gliding flight of ideal falcons predicts the motions of the falcons during gliding both with and without acceleration, and accelerating flight includes steep gliding (diving) up to vertical dives. The model partitions the total aerodynamic drag (D) into three parts:

$$D = D_{\mathrm{i}} + D_{\mathrm{pr}} + D_{\mathrm{par}}\,, \tag{2}$$

where D_{i} is the induced drag that arises when a wing produces lift, D_{pr} is the profile drag (the drag of the wing exclusive of the induced drag) and D_{par} is the parasite drag (the drag of the body exclusive of the wings). Partitioning drag in this way is conventional practice for manufactured aircraft, and Pennycuick (1968, 1971) introduced its use for gliding birds.

For birds, parasite drag is usually defined as the measured drag of wingless bodies in wind tunnels (Pennycuick et al., 1988; Tucker, 1990a). This definition tacitly assumes that there is no interference drag between the body and the wings when, in fact, the drag of the body with wings attached may differ from the total drag of the isolated body and isolated wings (Gesser et al., 1998; Hoerner, 1965; Nachtigall, 1998; Von Mises, 1959). The difference is the interference drag, which may be accounted for by adding it algebraically to the parasite drag.

The effect of parasite drag on the profile drag of ideal falcons

The profile drag of ideal falcons varies with the lift produced by the wings, and the relationship between these variables can be calculated from a 'polar curve for the wings', which shows the minimum profile drag coefficient ($C_{\mathrm{D,pr}}$) plotted against the lift coefficient (C_{L}) (Tucker, 1987). The profile drag used for the polar curve depends on parasite drag, since profile drag is left-over drag, i.e. the total drag minus the sum of induced drag and parasite drag. Thus, in the context of the polar curve, any change in measured parasite drag causes an equal and opposite change in profile drag, since there is no change in total and induced drag.

For example, Tucker (1987) derived a polar curve for the wings of a lugger falcon (*F. jugger*, similar in size and shape to a peregrine) at a Reynolds number of 50 000 based on wing chord:

$$C_{\mathrm{D,pr}} = 0.0349 - 0.0781C_{\mathrm{L}} + 0.0799C_{\mathrm{L}}^{2}\,. \tag{3}$$

The parasite drag from which this relationship was calculated came from measurements on frozen bodies and corresponds to a parasite drag coefficient ($C_{\mathrm{D,par}}$) of 0.37 (assuming S_{b} is that of an ideal falcon; Tucker, 1998). Later, Tucker (1990a) made new measurements of parasite drag and lowered $C_{\mathrm{D,par}}$ to 0.18. This value leads to a revised polar curve (Tucker, 1998):

$$C_{\mathrm{D,pr}} = 0.0512 - 0.084C_{\mathrm{L}} + 0.0792C_{\mathrm{L}}^{2}\,, \tag{4}$$

that gives higher $C_{\mathrm{D,pr}}$ values for any C_{L} because the reduction in parasite drag adds to the profile drag.

The drag measurements on the straight PF model in the present study suggest that $C_{\mathrm{D,par}}$ should be reduced again. Fig. 7 shows the effect of a range of $C_{\mathrm{D,par}}$ values on the polar curves for the same total and induced drag values used for equations 3 and 4. I shall refer to the curve for $C_{\mathrm{D,par}}$=0.1 again; the equation for this curve is:

$$C_{\mathrm{D,pr}} = 0.0761 - 0.1242C_{\mathrm{L}} + 0.0965C_{\mathrm{L}}^{2}\,. \tag{5}$$

The equation for the curve for $C_{\mathrm{D,par}}$=0.05:

$$C_{\mathrm{D,pr}} = 0.0828 - 0.1306C_{\mathrm{L}} + 0.0990C_{\mathrm{L}}^{2}\,, \tag{6}$$

may also be useful to readers who wish to use even lower values of $C_{\mathrm{D,par}}$, such as the value of 0.05 suggested by Pennycuick et al. (1996).

The effect of parasite drag on the gliding performance of a 1 kg ideal falcon

A changed value for $C_{\mathrm{D,par}}$ affects not only profile drag but also the gliding performance of an ideal falcon, as I shall illustrate with examples. The performance curves in the examples describe an ideal falcon with a body mass of 1 kg (equivalent to that of a large peregrine or a small gyrfalcon), a range of $C_{\mathrm{D,par}}$ values between 0.05 and 0.20 and polar curves for the wings from Fig. 7.

Fig. 8 shows a 'velocity polar diagram' (Tucker, 1998) for

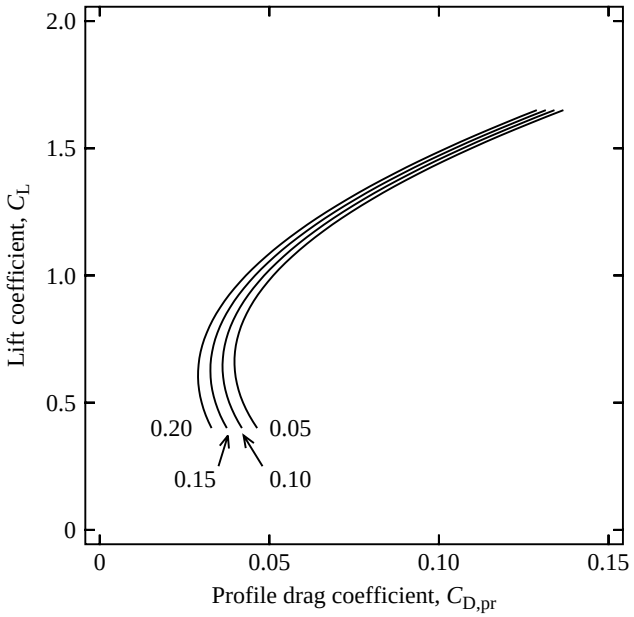

Fig. 7. Polar curves for the wings of a 1 kg ideal falcon with parasite drag coefficients between 0.05 and 0.20.

the gliding falcon. The four curves drawn with thick lines are 'maximum performance curves' for the range of $C_{D,par}$ values. A line on this diagram between the origin and a point on a maximum performance curve represents a two-dimensional velocity vector for the highest speed that the falcon can reach for that vector direction (the glide angle). Rays from the origin show glide angles, the axes show the horizontal and vertical components of the vector, and concentric circles show the magnitude (speed) of the vector. The maximum speed of the falcon at any glide angle depends markedly on $C_{D,par}$,

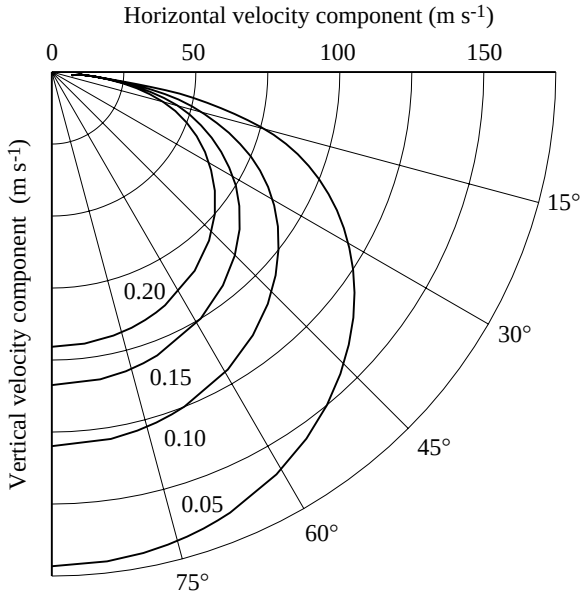

Fig. 8. A velocity polar diagram for a 1 kg ideal falcon with maximum performance curves for parasite drag coefficients between 0.05 and 0.20. See text for explanation.

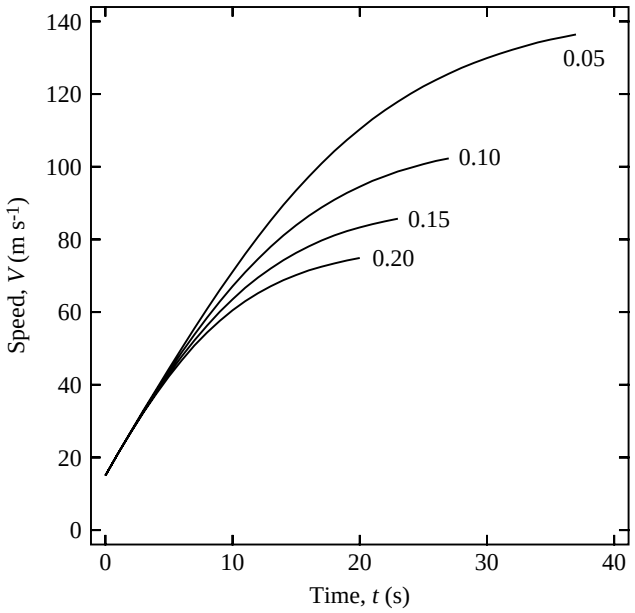

Fig. 9. The increase in speed with time for a 1 kg ideal falcon diving at 45° with parasite drag coefficients between 0.05 and 0.20. The curves end when the falcon has reached 95% of the speed shown by the corresponding curve for maximum performance in Fig. 8.

particularly at the steep angles and high speeds that occur during diving. Parasite drag becomes the largest component of drag at high speeds (Tucker, 1998), primarily because the falcon folds its wings as speed increases and reduces the wing area that generates profile drag.

Fig. 9 shows how the falcon's speed increases with time as it dives at 45° from a speed of 15 m s^{-1} to 95% of the speed at maximum performance. Again, the $C_{D,par}$ value has its greatest effect on a curve at the highest speeds, for the reasons mentioned above.

The extremely high speeds that the falcon could reach in a vertical dive, given enough space and time, are worth mentioning (in the 230–300 miles h^{-1} range in English units) for $C_{D,par}$ values of 0.1 or less. The body model measurements in the present study suggest that real falcons could have $C_{D,par}$ values in this range if $C_{D,par}$ decreases at high speeds because of Reynolds number effects, and there are reports of falcons reaching speeds above 200 miles h^{-1} (Tucker, 1998; Franklin, 1999).

Consequences of a turned head in the ideal falcon

Increase in drag and torque

The turned head of the bent PF body model causes changes in two measured quantities relative to the straight model: an increment in drag (ΔD) and an increment in torque. The bent model did not accelerate and change its position perceptibly in response to these increments because the mounting strut provided equal and opposite compensating forces and torques, but a gliding bird lacks a strut. The bird can avoid acceleration when it turns its head only by altering its body shape or flight path to produce compensating forces and torques from

gravitational components or aerodynamic forces. Thus, it incurs both the drag increment ΔD measured on the bent body model and the drag D_T that accompanies the generation of the compensating torque.

Torque compensation by yawing

In one case, ΔD describes the bent PF model with no net torque acting on it – when the model is yawed 11.6° in the opposite direction to that in which the head is turned (Fig. 6). ΔD for the model at this yaw angle is 1.45 times the drag on the straight model at yaw and pitch angles of 0°.

However, this method for torque compensation would be counter-productive for a real falcon that turns its head in an attempt to direct the line of sight for maximum visual acuity of one eye along the flight path. Yawing would swing the line of sight back towards where it started, and the falcon would have to turn its head even more. That motion would again increase torque, and the falcon would have to yaw even more to compensate. Eventually, the falcon might reach equilibrium with its head turned more than 40°, but at an unknown value for ΔD.

Torque models for the drag from torque compensation

In this section, the ideal falcon turns its head and generates compensating forces equal to ΔD and D_T to keep from accelerating. I shall estimate ΔD from measurements on the PF model bodies, and use three torque models to estimate D_T. These models make several assumptions for which there is little supporting evidence, but the calculations do show how compensating torque may arise from adjustments in body shape, and they also provide estimates of how large D_T might be.

Definition of torque and moment arm. Torque (**T**, in bold type to indicate a vector) is the vector product of a force (**F**) and the displacement (**d**) between the point of application of **F** and the torque axis, along which the torque vector is directed. This paper refers only to the magnitude of torque (T), force (F) and distance (d), and:

$$T = Fd\sin\alpha\,, \tag{7}$$

where F is the magnitude of **F**, α is the angle between **F** and **d**, and $d\sin\alpha$ is the component of **d** perpendicular to **F** known as the 'moment arm' (M). For example, when **F** is in the direction of drag, M is perpendicular to the direction of air flow around the bird, and when **F** is in the direction of lift (i.e. perpendicular to the direction of air flow), M is parallel to the direction of air flow. The bird can generate torque from either drag or lift when these components act on moment arms. The first torque model describes torque generated by drag, and the next two describe torque generated by lift.

Assumptions of the torque models. All three models describe the 1 kg ideal falcon diving at an angle of 45° in an atmosphere with a density (ρ) of 1.23 kg m^{-3}. The falcon's speed is 70 m s^{-1}, and its wing span (b) at this speed is 0.122 m. The falcon dives with its head straight and then turns its head, thereby increasing its parasite drag and torque. It simultaneously adjusts some other part of its body to generate a compensating torque that prevents yawing, and each torque model specifies the ratio (R_{par}) of the drag after and before head-turning:

$$R_{par} = (D_{par,s} + \Delta D + D_T)/D_{par,s}\,, \tag{8}$$

where $D_{par,s}$ is the parasite drag with the head held straight.

The three models make several assumptions about quantities for which few or no measurements on birds are available, and three of these assumptions are used in all the models. (i) The falcon's parasite drag coefficient is 0.1 when its head is straight; and the drag increment ΔD when it turns its head is calculated from the difference between the drag coefficients of the bent and straight PF model bodies at yaw and pitch angles of 0°. (ii) Drag coefficients do not change with Reynolds number; hence, drag is proportional to V^2. This assumption is correct over small ranges of Reynolds number, but it probably overestimates drag as Reynolds number increases. (iii) The torque that arises when the falcon turns its head can be calculated from a torque coefficient (C_T) that does not change with Reynolds number:

$$C_T = 2T/(\rho S_h M V^2)\,, \tag{9}$$

where S_h is a cross-sectional surface area of the head.

The torque on the ideal falcon with its head turned is greater than that on the bent PF body model, because the ideal falcon is bigger (m=1 kg, where m is body mass) than the PF (m=0.713 kg) from which the body model was made. Since the product S_hM is proportional to body mass, the torque on the ideal falcon at 11.7 m s^{-1} is 1/0.713 times that on the bent PF body model at pitch and yaw angles of 0°, and is proportional to V^2.

Torque model 1: torque due to drag. In this model, the falcon generates a compensating torque T by increasing the drag of one wing by D_T, which acts on a moment arm that is perpendicular to the midsagittal plane. Since the compensating torque is D_TM:

$$D_T = T/M\,, \tag{10}$$

and, from assumptions ii and iii, the ratio R_{par} (from equation 8) is constant with speed.

For example, assuming that M is b/2 (i.e. 0.061 m), then R_{par}=6.5. That is, turning the head in flight multiplies the parasite drag of the straight body by this ratio. This example estimates a relatively large value for D_T, since R_{par}=1.6 when D_T is zero.

Torque model 2: torque due to wing lift. In this model, the falcon holds its wings cupped near its sides, so that the wings have surfaces parallel to the midsagittal plane and can produce 'lateral lift' (L_L) perpendicular to this plane (Tucker, 1998). Franklin (1999) shows photographs of a real falcon in this position, taken by a photographer falling through the sky with the falcon. The ideal falcon generates a compensating torque by producing lateral lift with one wing, with the moment arm parallel to the body axis. The compensating torque is L_LM, and:

$$L_L = T/M\,. \tag{11}$$

The drag D_T that accompanies L_L is entirely due to the increased induced drag of the wings (neglecting any profile

drag increase), and the induced drag of the wings with an elliptical lift distribution is:

$$D_i = 2(L + L_L)^2/(\pi\rho V^2 b^2), \quad (12)$$

where L is the lift that supports the falcon's weight (for a more complete discussion of induced drag, see Tucker, 1987; Pennycuick, 1989; and aerodynamics texts). In a 45° dive:

$$L = mg\cos 45°, \quad (13)$$

where m is the falcon's body mass, and g is the magnitude of gravitational acceleration (9.81 m s^{-2}).

The induced drag of the ideal falcon will exceed that calculated from equation 12 because the lift distribution along the wing, including L_L, is not elliptical. Thus, D_T exceeds the increment ΔD_i:

$$\Delta D_i = 2[(L + L_L)^2 - L^2]/(\pi\rho V^2 b^2) = 2(2LL_L + L_L^2)/(\pi\rho V^2 b^2). \quad (14)$$

For example, if M is b/5 (i.e. 0.024 m), then R_{par}>5.5.

Torque model 3: torque due to tail lift. In this model, the falcon holds its tail twisted and slightly spread to a span of b at the distal end and produces lift (L) inclined at 30° to the midsagittal plane. The lateral component (L_L) of L perpendicular to the plane is:

$$L_L = L\sin 30°. \quad (15)$$

The moment arm for this torque is parallel to the body axis, and:

$$L = T/(M\sin 30°). \quad (16)$$

The drag D_T that accompanies L is entirely induced drag from the tail (again neglecting profile drag) and, for an elliptical lift distribution:

$$D_i = 2L^2/(\pi\rho V^2 b^2). \quad (17)$$

(for a detailed analysis of tail aerodynamics, see Thomas, 1993). From assumptions ii and iii, both L and D_i are proportional to V^2, and R_{par} is constant with speed. For a non-elliptical lift distribution, D_T>D_i.

For example, if M is 2b (i.e. 0.244 m), then R_{par}>1.7. This value for R_{par} indicates a relatively small value for D_T compared with R_{par}=1.6 when D_T is zero. However, a falcon probably does not have a stiff enough tail to produce the entire compensating torque by this method, because the required lift on the tail at 70 m s^{-1} is 56% of the ideal falcon's weight. When I loaded the end of a dead peregrine's tail with a force equal to one-quarter of the falcon's weight, the tail feathers bent abnormally from a horizontal position at the base to 40° below horizontal at the point of loading.

Effect of a turned head on the total drag

The increased parasite drag ΔD+D_T that accompanies head-turning is only one component of total drag (equation 2), and it is an increasing proportion of total drag as speed increases. This effect may be quantified with the ratio R_{tot}:

$$R_{tot} = D'/D, \quad (18)$$

where D' is the total drag of the ideal falcon with its head turned and D is its total drag with its head straight. Fig. 10 shows the relationship between R_{tot} and speed for values of the ratio R_{par} between 1 and 4. For example, if R_{par}=2, which is close to the value from torque model 3, the total drag of the falcon would be multiplied by a value for R_{tot} of 1.20 at a speed of 20 m s^{-1} and by 1.78 at a speed of 70 m s^{-1}. Thus, head-turning has a relatively small effect on gliding performance at low speeds, but it could markedly slow down the bird at high speeds.

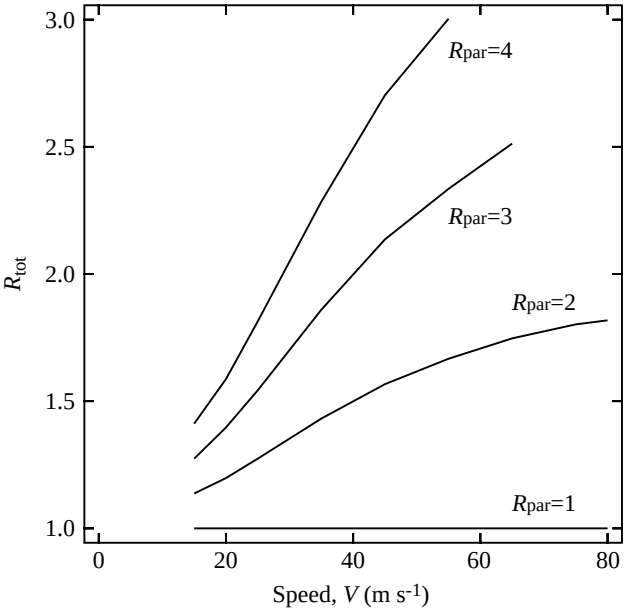

Fig. 10. Ratios of drag of a 1 kg ideal falcon with a turned head to that with a straight head when the falcon dives at a range of speeds and an angle of 45°. The ratio (R_{par}) for parasite drag may be between 1 and 4, as shown by the four curves. The ratios for total drag (R_{tot}; shown on the vertical axis) are always less than R_{par} at a given speed, because parasite drag is only part of total drag. For example, if the parasite drag doubles when the falcon turns its head in a dive at 70 m s^{-1}, the total drag increases by a factor of 1.78.

Real raptors commonly turn their heads while gliding slowly, probably to change their line of sight and to initiate or control yawing. However, I do not remember seeing a falcon turn its head in a high-speed dive, and Fig. 10 suggests why: raptors probably pay an increasing speed penalty for head-turning as speed increases. For example, the torque models for head-turning show that the parasite drag coefficient could plausibly more than double if a falcon turned its head at 70 m s^{-1}, and doubling the parasite drag coefficient has a marked effect on the velocity polar diagram and the acceleration during a dive (Figs 8, 9).

Thus, to summarize this discussion of turned heads and the conflict between the requirements for acute vision and high-speed flight: if diving raptors turn their heads in a dive to view the prey straight ahead with maximum acuity, they will incur a substantial speed penalty from increased drag. Tucker (2000) shows show how they could avoid this penalty by approaching the prey along a spiral path.

The parasite drag of real raptors

Several mathematical models predict the motions and energy requirements of flapping birds (for reviews, see Pennycuick, 1989; Rayner, 1999) and gliding birds (Tucker, 1998). For a given bird, these models use a constant value for the parasite drag coefficient ($C_{D,par}$). This value usually comes from measurements made on wingless bird bodies in wind tunnels, since a direct method is not available for measuring the parasite drag of a flying bird. However, a single value for $C_{D,par}$ measured in this way is only an approximation for a real bird for two reasons: first, $C_{D,par}$ may vary in flight with yaw and pitch angles and head position (present study) or with Reynolds number (Tucker, 1998); and second, how accurately the measured values describe a living bird is unknown. There are reasons to suspect that the accuracy is low (see below), yet values of $C_{D,par}$ measured in wind tunnels make useful predictions of the behavior of birds in flight.

Some authors have recently suggested another method for determining $C_{D,par}$: choose a value that improves the accuracy of the mathematical model. Pennycuick et al. (1996) used a mathematical model (Pennycuick, 1989) that predicted flight speeds from $C_{D,par}$ and other assumed values, and then adjusted $C_{D,par}$ to match the predicted speeds with those observed in a bird flying in a wind tunnel. They suggested reducing the $C_{D,par}$ values in the original model by a factor of up to 8 (to give $C_{D,par}$ as low as 0.05) to make the model more accurate.

Tucker et al. (1998) used a similar approach and compared the predictions of a mathematical model for diving falcons (Tucker, 1998) with speeds measured during dives at various angles by a gyrfalcon. The predictions matched the measured values more closely with a $C_{D,par}$ of 0.07, rather than the value of 0.18 estimated from wind tunnel measurements. At least part of this difference could be due to Reynolds number effects, since the wind tunnel speeds were less than one-quarter of those reached by the gyrfalcon.

Ideally, the two methods for determining $C_{D,par}$ would yield the same result, but both methods depend on several uncertain assumptions. Here, I discuss the uncertainties in determining $C_{D,par}$ from measurements in wind tunnels and then suggest a compromise value for $C_{D,par}$ that bridges the gap between the results of the two methods.

One of the differences between a living bird body and a model body is that the feathers of the bird are a compliant surface whose shape may be controllable by the bird. For example, a perched hawk obviously changes the thickness of its feathers as it fluffs them and swells up or compresses them to become sleek and slender. In flight, such changes may influence the boundary layer of air around the body and also the distribution of air pressure on the body. Both these changes may change $C_{D,par}$ (Du and Karniadakis, 2000; Tucker, 1990a).

Some wind tunnel studies show how feathers could influence parasite drag. In this paper, the drag coefficient of the laminated body model was more than 25 % higher than that of the straight PF model made from the same set of surface points because the laminated model had shallow concavities on its surface. Eliminating these concavities, particularly those around the thighs, made the drag coefficients equal, and the feathers of living birds may fill in such concavities.

Nachtigall (1998) compared the drag coefficients of a starling (*S. vulgaris*) gliding in a wind tunnel with those of a smooth model on a drag balance. The minimum drag coefficient of the living bird was lower than that of the model, and Nachtigall (1998) attributed the difference to the presence of feathers. The model itself had an exceptionally low minimum drag coefficient (0.08 with the wings removed) compared with a minimum drag coefficient of 0.11 for the straight PF body model in this study.

However, frozen bird bodies in wind tunnels have a higher drag than smooth models, probably partly because the feathered surface of a frozen body is not as smooth that of a living bird in flight (Tucker, 1990a). A frozen, feathered body had 70 % more drag than a smooth plaster model of the same body (Tucker, 1990a), and Pennycuick et al. (1988) reduced the drag on a frozen body by 15 % by smoothing the feathers and holding them in place with hair spray.

Measurements on frozen bodies probably overestimate the drag of living birds, and this suggestion is consistent with an evolutionary argument: that the lowest C_D that can be measured on a reasonably anatomically correct smooth model could also occur in a living bird with naturally arranged feathers, given the many other refined avian characters for flight produced by the evolutionary process.

However, the drag of isolated body models, feathered or smooth, might underestimate the drag of the same body attached to the wings of a living bird, because a measurement on an isolated body does not include the interference drag between the body and the wings (Gesser et al., 1998; Hoerner, 1965; Nachtigall, 1998; Von Mises, 1959). Or, the presence of the wings might reduce drag by preventing flow separation around the body. These uncertainties cause Pope and Harper (1966, p. 269) to question the value of drag measurements on a wingless aircraft fuselage without information on interference drag.

Taking all the evidence together, the value for $C_{D,par}$ of 0.1 used for the ideal falcon in this paper appears to be a reasonable compromise for gliding raptors, together with the relationship between $C_{D,pr}$ and C_L given by equation 5. Historically, $C_{D,par}$ has declined as new methods have been developed for measuring drag in wind tunnels and as data have accumulated on the accuracy of mathematical flight models. Now, the results from measurements and mathematical models seem remarkably close, considering the difference in the methodologies.

List of symbols

AC	armature-cutting
b	wing span
C_1, C_2, C_3	coefficients of parabolic equations
C_D	drag coefficient of body models, usually a minimum
$C_{D,par}$	parasite drag coefficient
$C_{D,pr}$	profile drag coefficient

C_L	lift coefficient
C_T	torque coefficient
D	total drag
D'	total drag of the ideal falcon with a turned head
D_i	induced drag
D_{par}	parasite drag
$D_{par,s}$	parasite drag with a straight head
D_{pr}	profile drag
D_T	drag to compensate for torque
d	magnitude of displacement
d	displacement vector
F	magnitude of force
F	force vector
g	magnitude of gravitational acceleration
L	lift
L_L	lateral lift
m	body mass
M	moment arm
PF	peregrine falcon
RT	red-tailed hawk
R_{par}	ratio of parasite drag values before and after head-turning
R_{tot}	ratio of total drag values with head turned and straight
r	radius for cylindrical coordinates
S_b	maximum area of a body section
S_h	cross-sectional area of the head
T	magnitude of torque
T	torque vector
t	time
V	speed through the air
x	pitch or yaw angle
y	parasite drag coefficient or head angle
z	axis for cylindrical coordinates
α	angle between force and displacement for torque
Δ	change in a quantity
Θ	angle for cylindrical coordinates
π	ratio of circumference to diameter of a circle
ρ	air density

This study was partially supported by a grant (DEB-9107222) from the National Science Foundation.

References

Du, Y. and Karniadakis, G. E. (2000). Suppressing wall turbulence by means of a transverse traveling wave. *Science* **288**, 1230–1234.

Franklin, K. (1999). Vertical flight. *North Am. Falconers' Ass. J.* **38**, 68–72.

Gesser, R., Wedekind, F., Kockler, R. and Nachtigall, W. (1998). Aerodynamische Untersuchungen an naturnahen Starenmodellen. 2. Flügel-Rumpf-Interferenzen. In *Biona Report* **13**, *Motion Systems* (ed. R. Blickhan, A. Wisser and W. Nachtigall), pp. 257–258. Stuttgart: Fischer.

Hoerner, S. F. (1965). *Fluid-dynamic Drag*. Brick Town, NJ: S. F. Hoerner.

Nachtigall, W. (1998). Starling and starling models in wind tunnels. *J. Avian Biol.* **29**, 478–484.

Pennycuick, C. J. (1968). A wind-tunnel study of gliding flight in the pigeon *Columba livia*. *J. Exp. Biol.* **49**, 509–526.

Pennycuick, C. J. (1971). Control of gliding angle in Rüppel's griffon vulture *Gyps rueppellii*. *J. Exp. Biol.* **55**, 39–46.

Pennycuick, C. J. (1989). *Bird Flight Performance*. New York: Oxford Press.

Pennycuick, C. J., Klaassen, M., Kvist, A. and Lindström, Å. (1996). Wingbeat frequency and the body drag anomaly: wind tunnel observations of a thrush nightingale (*Luscinia luscinia*) and a teal (*Anas crecca*). *J. Exp. Biol.* **199**, 2757–2765.

Pennycuick, C. J., Obrecht, H. H. and Fuller, M. R. (1988). Empirical estimates of body drag of large waterfowl and raptors. *J. Exp. Biol.* **135**, 253–264.

Pope, A. and Harper, J. J. (1966). *Lowspeed Wind Tunnel Testing.* New York: Wiley & Sons.

Rayner, J. M. V. (1999). Estimating power curves of flying vertebrates. *J. Exp. Biol.* **202**, 3449–3461.

Thomas, A. L. R. (1993). On the aerodynamics of birds' tails. *Phil. Trans. R. Soc. B* **346**, 361–380.

Tucker, V. A. (1987). Gliding birds: the effect of variable wing span. *J. Exp. Biol.* **133**, 33–58.

Tucker, V. A. (1990a). Body drag, feather drag and interference drag of the mounting strut in a peregrine falcon *Falco peregrinus*. *J. Exp. Biol.* **149**, 449–468.

Tucker, V. A. (1990b). Measuring aerodynamic interference drag between a bird body and the mounting strut of a drag balance. *J. Exp. Biol.* **154**, 439–461.

Tucker, V. A. (1998). Gliding flight: speed and acceleration of ideal falcons during diving and pull out. *J. Exp. Biol.* **201**, 403–414.

Tucker, V. A. (2000). The deep fovea, sideways vision and spiral flight paths in raptors. *J. Exp. Biol*. **203**, 3745–3754.

Tucker, V. A., Cade, T. J. and Tucker, A. E. (1998). Diving speeds and angles of a gyrfalcon (*Falco rusticolus*). *J. Exp. Biol.* **201**, 2061–2070.

Tucker, V. A. and Parrott, G. C. (1970). Aerodynamics of gliding flight in a falcon and other birds. *J. Exp. Biol.* **52**, 345–367.

Tucker, V. A., Tucker, A. E., Akers, K. and Enderson, J. H. (2000). Curved flight paths and sideways vision in peregrine falcons (*Falco peregrinus*). *J. Exp. Biol.* **203**, 3755–3763.

Von Mises, R. (1959). *Theory of Flight*. New York: Dover Publications.